

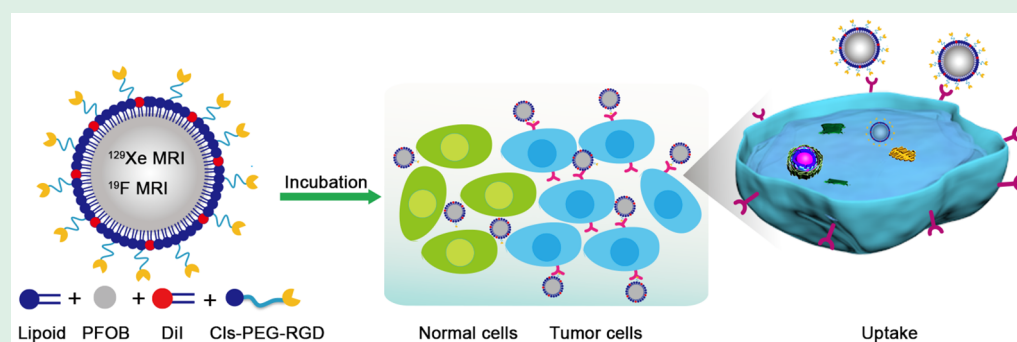
# $^{129}\text{Xe}$ Hyper-CEST/ $^{19}\text{F}$ MRI Multimodal Imaging System for Sensitive and Selective Tumor Cells Detection

Huaibin Zhang,<sup>†,‡,§</sup> Shizhen Chen,<sup>†,‡</sup> Yaping Yuan,<sup>‡</sup> Yu Li,<sup>§</sup> ZhongXing Jiang,<sup>\*,§,†</sup> and Xin Zhou<sup>\*,‡,†</sup>

<sup>†</sup>State Key Laboratory for Magnetic Resonance and Atomic and Molecular Physics, National Center for Magnetic Resonance in Wuhan, Wuhan Institute of Physics and Mathematics, Chinese Academy of Sciences, Wuhan 430071, China

<sup>§</sup>Hubei Province Engineering and Technology Research Center for Fluorinated Pharmaceuticals and School of Pharmaceutical Sciences, Wuhan University, Wuhan 430071, China

## S Supporting Information



**ABSTRACT:** Heteronuclear MRI offers broad potential for specific detection and quantification of molecularly targeted agents in diagnosis and therapy planning or monitoring. Here we report a novel method for simultaneous acquisition of dual-nuclei hyper-CEST  $^{129}\text{Xe}$  and  $^{19}\text{F}$  tumor targeting MRI.  $^{129}\text{Xe}$  hyper-CEST MRI,  $^{19}\text{F}$  MRI and fluorescent imaging were integrated into PFOB nanoemulsion as a imaging system for sensitive and selective tumor cells detection. As the complement to  $^1\text{H}$  MRI,  $^{129}\text{Xe}$  and  $^{19}\text{F}$  signals can also provide efficient and precise anatomical localization of tumors.

**KEYWORDS:** nanoemulsion, hyper-CEST,  $^{129}\text{Xe}$  MRI,  $^{19}\text{F}$  MRI, tumor

Detecting tumors on cellular and molecular levels with imaging technologies is of great importance for early diagnosis and efficient treatment of cancer. As one of the most used imaging technologies in oncology, proton magnetic resonance imaging ( $^1\text{H}$  MRI) detects the proton relaxation difference in body water and provides tumor images with high spatial resolution.<sup>1–3</sup> However,  $^1\text{H}$  MRI lacks of sensitivity for detecting low-abundance biomolecular markers of cancer. To address this issue, hyperpolarized  $^{129}\text{Xe}$  MRI has emerged as an attractive complementary technology.<sup>4,5</sup> The hyperpolarized  $^{129}\text{Xe}$ , which can be produced by a home-built continuous-flow apparatus, can increase the MRI sensitivity by more than 10 000-fold.<sup>6–8</sup> Beyond hyperpolarization, a further over 100-fold sensitivity enhancement can be achieved by using a novel indirect detection technology named Hyper-CEST.<sup>9–11</sup> So,  $^{129}\text{Xe}$  hyper-CEST MRI can meet the sensitivity requirement in oncology applications. Besides,  $^1\text{H}$  MRI also suffers the low selectivity issue of differentiating the tumor tissues from normal tissues due to huge background signals. To this end,  $^{19}\text{F}$  MRI complements  $^1\text{H}$  MRI by providing images without background signal.<sup>12–14</sup> Therefore,  $^{129}\text{Xe}$  hyper-CEST MRI and  $^{19}\text{F}$  MRI may be effective imaging technologies for sensitively and selectively tumor detecting on cellular and molecular levels.

Multimodal imaging systems take the advantage of each imaging technology and provide detailed multidimensional information simultaneously for accurate cancer diagnosis and therapy.<sup>15–17</sup> Constructing a multimodal imaging system with the high sensitivity of  $^{129}\text{Xe}$  hyper-CEST MRI, the high selectivity of  $^{19}\text{F}$  MRI, and the convenience of fluorescent imaging would be highly valuable. However, as far as we know, there is no report on such imaging system. It is noteworthy that many gases, including  $^{129}\text{Xe}$ , are highly soluble in perfluorocarbons (PFCs).<sup>18–20</sup> The high sensitivity of  $^{129}\text{Xe}$  has facilitated the detection of  $^{129}\text{Xe}$  hyper-CEST signal in PFOB nanoemulsion at pM level.<sup>21,22</sup> Recently, perfluorocarbons (PFCs) nanoemulsions have been widely used as  $^{19}\text{F}$  MRI probes and cell tracers in biomedical research because of their easy availability and high  $^{19}\text{F}$  MRI signal.<sup>23–25</sup> Therefore, it is feasible to integrate  $^{129}\text{Xe}$  hyper-CEST MRI and  $^{19}\text{F}$  MRI into a PFCs nanoemulsion-based multimodal imaging system.

Herein, we report a PFCs nanoemulsion-based multimodal imaging system with  $^{129}\text{Xe}$  hyper-CEST MRI,  $^{19}\text{F}$  MRI, and fluorescent imaging for sensitive and selective tumor cells

**Received:** October 22, 2018

**Accepted:** December 19, 2018

**Published:** December 19, 2018

## Scheme 1. Multimodal Imaging System for Tumor Detection

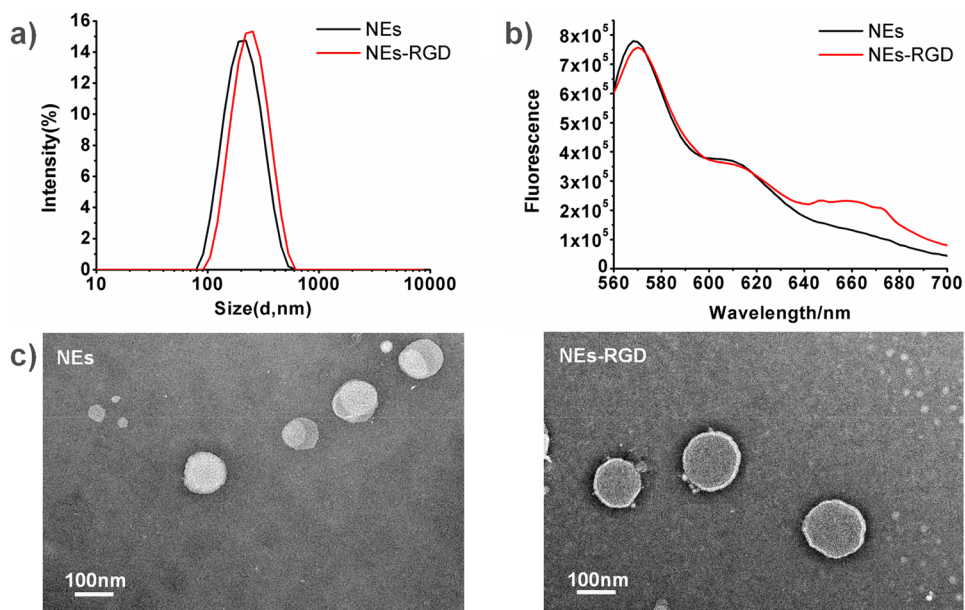
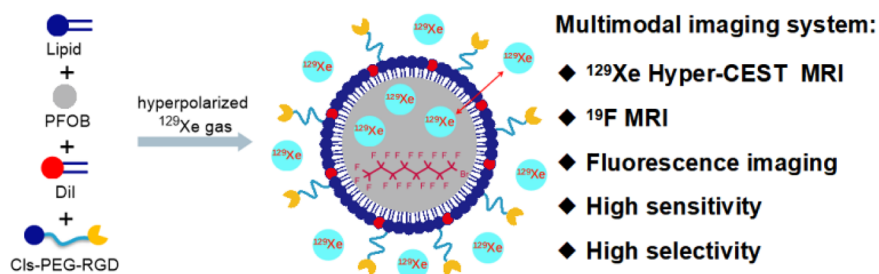


**Figure 1.** (a) DLS, (b) fluorescent emission spectrum, (c) TEM (left: NEs; right: NEs-RGD) of fluorinated nanoemulsions.

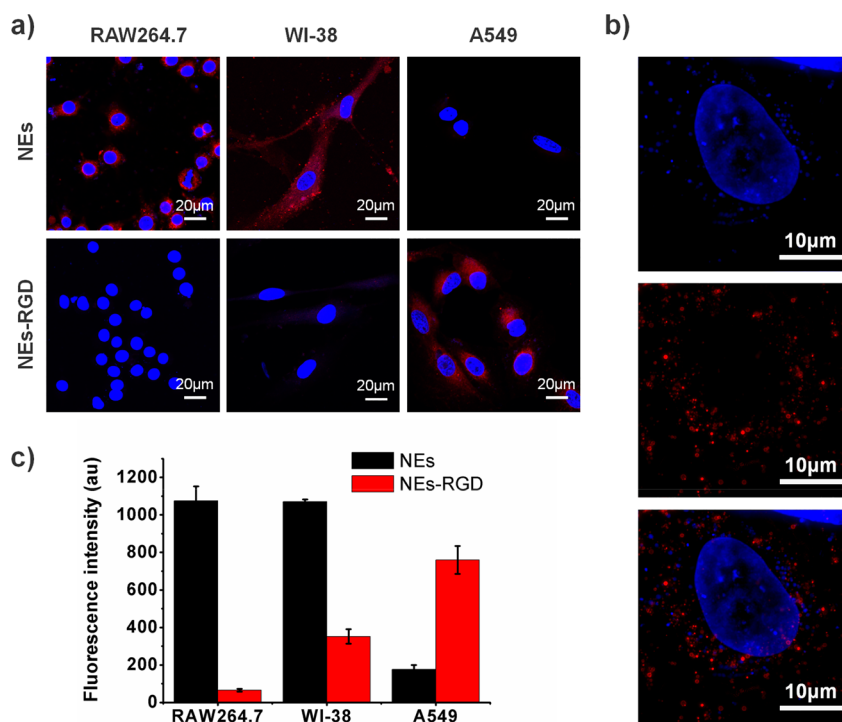


**Figure 2.** (a) Confocal images of NEs or NEs-RGD treated RAW264.7 cells, A549 cells, and WI-38 cells (b) structure illumination microscopy images of NEs-RGD treated A549 cells and (c) fluorescence intensity of NEs or NEs-RGD treated RAW264.7 cells, A549 cells, and WI-38 cells.

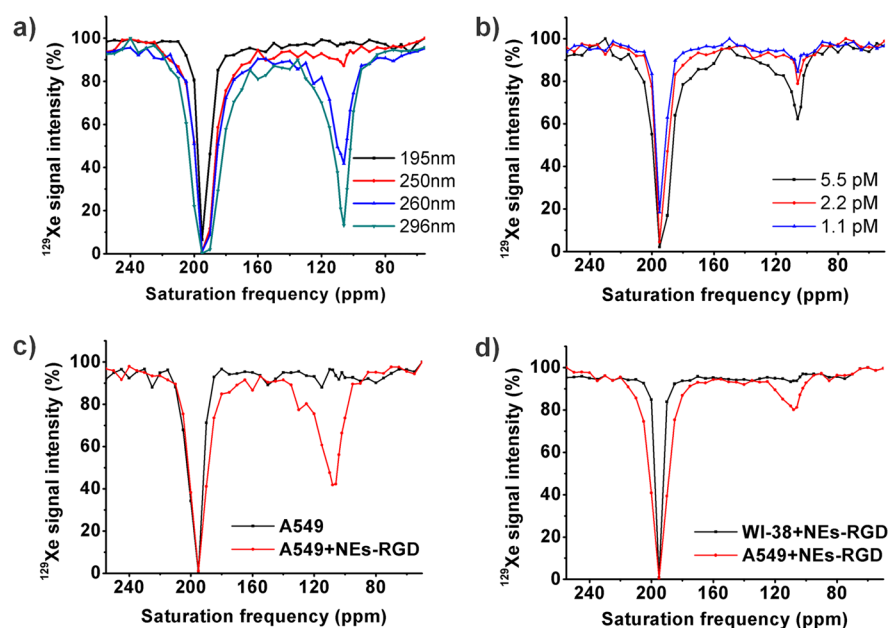


**Figure 3.**  $^{129}\text{Xe}$  Z-spectrum of  $^{129}\text{Xe}$ -treated NEs of (a) different sizes, (b) concentrations, (c) A549 cells and NEs-RGD treated A549 cells, (d) NEs-RGD treated A549 cells and WI-38 cells.

detection (Scheme 1). Perfluorooctyl bromide (PFOB) nanoemulsion with phospholipids as emulsifier is employed as the platform for the imaging system. In the nanoemulsion, a large amount of  $^{19}\text{F}$  with similar chemical shift in PFOB collectively produces a strong  $^{19}\text{F}$  signal for sensitive  $^{19}\text{F}$  MRI. To incorporate fluorescent imaging, we anchored fluorescent dye DiI on the phospholipid surface of the nanoemulsion.<sup>21</sup> In the same way, cholesterol-labeled targeting peptide Cls-PEG-RGDyc is incorporated to achieve targeted imaging of cancerous cells that have a high expression of integrin  $\alpha v\beta 3$ . Under an environment of hyperpolarized  $^{129}\text{Xe}$ , the high solubility of  $^{129}\text{Xe}$  in PFOB promotes the diffusion of  $^{129}\text{Xe}$  from the aqueous phase to  $^{19}\text{F}$ -containing phase. Because the chemical shift of  $^{129}\text{Xe}$  is highly sensitive to the environment,<sup>26–28</sup> a new  $^{129}\text{Xe}$  signal from the dissolved  $^{129}\text{Xe}$  in PFOB would be produced. With the exchangeable hyperpolarized  $^{129}\text{Xe}$  between the aqueous phase and the  $^{19}\text{F}$ -containing phase,  $^{129}\text{Xe}$  hyper-CEST MRI is feasible to detect the PFOB nanoparticles with high sensitivity and selectivity. Through the multimodal imaging system, selective and sensitive tumor information may be obtained for accurate cancer diagnosis and therapy.

PFOB nanoemulsion (NEs) were then formulated with Pluronic F-68 and Lipoid S75 as the emulsifiers. Dynamic light scattering (DLS) showed the hydrodynamic diameters of NEs as 195 nm with a polydispersity index (PDI) of 0.19 and a zeta potential ( $\zeta$ ) of  $-12.9 \pm 0.9$  mV (Figure 1a). Fluorescent dye DiI was self-assembled onto the nanoparticle surface through hydrophobic interactions which provided a maximum fluorescent emission around 570 nm (Figure 1b). To achieve tumor targeting, we incorporated Cls-PEG-RGDyc, which was synthesized through a click reaction between mercapto and maleimide, into the nanoemulsion. The resulting nanoemulsion NEs-RGD is slightly larger than NEs because of the surface modification by Cls-PEG-RGD (Figure 1a, c). It is noteworthy that a series of nanoemulsions with different sizes were prepared by tuning the ratio between PFOB and

phospholipid and sonicating or extruding the emulsion through membrane (detailed in the Supporting Information).

Fluorescent imaging was first employed to investigate the nanoemulsions' cancer cells selectivity. Laser confocal microscopy images showed big differences in cellular uptake selectivity between nanoemulsions NEs and NEs-RGD (Figure 2a, b). Interestingly, high uptake by normal human lung cells (WI-38) and murine macrophage (RAW 264.7) and neglectable uptake by human lung cancer cells (A549) were observed in NEs treated cells. High uptake was only observed in NEs-RGD treated A549 cells. After being blocked with RGD molecule, the A549 cells shows low uptake of NEs-RGD (Figure S5). The result reflects that high cancer cell selectivity of NEs-RGD is a result of molecular recognition between targeting peptide RGDyc and overexpressed integrin  $\alpha v\beta 3$  in A549 cells. The stealthy effect of PEGs may hamper the NEs-RGD uptake by WI-38 cells and RAW 264.7 cells. Structure illumination microscopy indicated that nanoemulsion NEs-RGD was evenly distributed in the cytoplasm of A549 cells (Figure 2c). MTT cytotoxicity assay on A549 cells and human breast cancer cells (MCF-7) showed low toxicity of NEs and NEs-RGD (Figure S6).

To prove the feasibility of  $^{129}\text{Xe}$  hyper-CEST MRI, we investigated  $^{129}\text{Xe}$  Z-spectrum of  $^{129}\text{Xe}$ -treated nanoemulsions NEs and NEs-RGD. Beside the aqueous  $^{129}\text{Xe}$  signal at 195 ppm, a CEST signal from exchangeable  $^{129}\text{Xe}$  in the fluorine phase is crucial for achieving  $^{129}\text{Xe}$  hyper-CEST MRI. The Z-spectrum of  $^{129}\text{Xe}$ -treated NEs indeed showed a new signal at 106 ppm from the PFOB-dissolved  $^{129}\text{Xe}$ . But the signal intensity is highly dependent on the particle size of NEs, i.e., an obvious signal can be detected when particle size is larger than 250 nm. It is probably because the smaller NEs have a faster chemical exchange (Figure 3a). Even at pM level, the NEs concentration-dependent  $^{129}\text{Xe}$  CEST signal intensity was observed (Figure 3b). On cellular level, the  $^{129}\text{Xe}$  CEST effects showed high cells selectivity. On the one hand, only NEs-RGD-treated A549 cells can generate the  $^{129}\text{Xe}$  CEST signal and no  $^{129}\text{Xe}$  CEST signal was observed from A549 cells alone

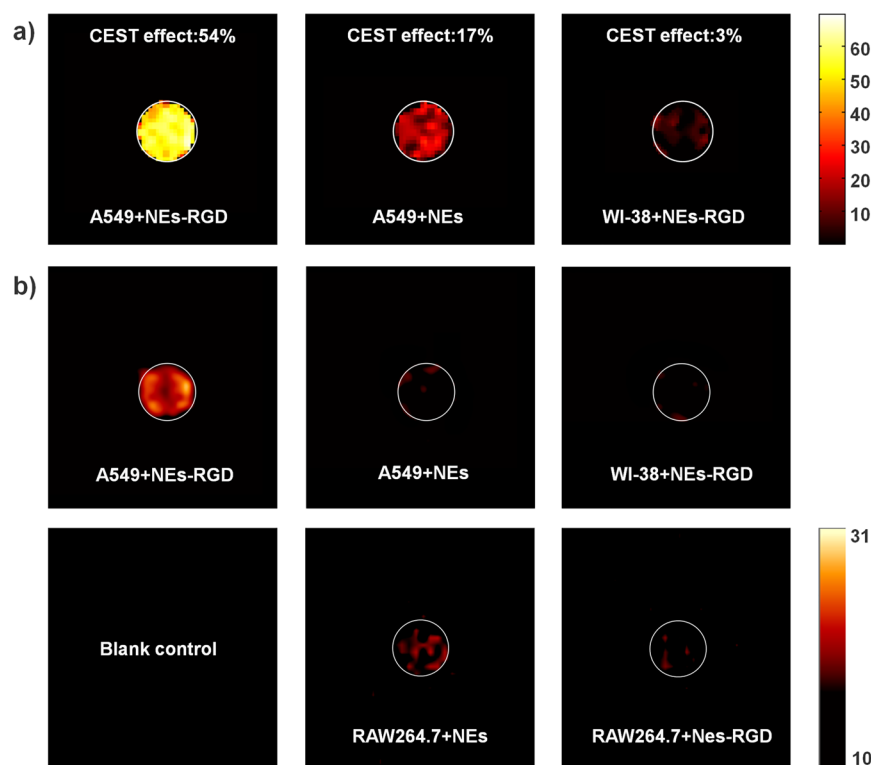


**Figure 4.** (a)  $^{129}\text{Xe}$  hyper-CEST MRI and (b)  $^{19}\text{F}$  MRI of NEs or NEs-RGD-treated A549 cells, WI-38 cells, and RAW264.7 cells as indicated.

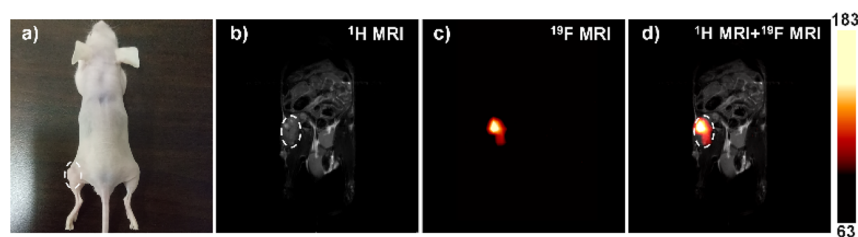


**Figure 5.** (a) Photo, (b)  $^1\text{H}$  MRI, (c)  $^{19}\text{F}$  MRI, and (d) overlay of  $^1\text{H}$  MRI and  $^{19}\text{F}$  MRI of an A549 xenograft nude mouse with NEs-RGD intratumoral injection.

(Figure 3c). On the other hand, the  $^{129}\text{Xe}$  CEST signal was not found in NEs-RGD-treated WI-38 cells but in NEs-RGD-treated A549 cells (Figure 3d). Therefore, PFCs nanoemulsion provide a perfect platform for generating  $^{129}\text{Xe}$  CEST signal and Cls-PEG-RGD modification of the nanoemulsion achieves high cancer cells selectivity for potential  $^{129}\text{Xe}$  hyper-CEST MRI.

$^{129}\text{Xe}$  hyper-CEST MRI and  $^{19}\text{F}$  MRI dual-image for selective detection of cancer cells were carried out. First,  $^{129}\text{Xe}$  hyper-CEST MRI shows high selectivity on NEs-RGD treated A549 cells (Figure 4a). With a RARE sequence, NEs-RGD (diameter of 200 nm) treated A549 cells showed a high CEST signal of 54%, while NEs treated A549 cells showed a CEST enhancement of only 17%. Under the same condition, NEs-RGD treated WI-38 cells showed a neglectable CEST enhancement of 3%. Second,  $^{19}\text{F}$  MRI shows even higher selectivity on these cells (Figure 4b). A clear image was obtained from  $^{19}\text{F}$  MRI of NEs-RGD-treated A549 cells, whereas very obscure images were obtained from either NEs treated A549 cells or NEs-RGD-treated WI-38 cells. Third, the  $^{19}\text{F}$  MRI of RAW264.7 cells after being treated with NEs and NEs-RGD once again shows that PEGylation may reduce the NEs-RGD uptake by RAW 264.7 cells. These results are

consistent with the fluorescent images and  $^{129}\text{Xe}$  Z-spectrum of cells. In the study,  $^{129}\text{Xe}$  hyper-CEST MRI and  $^{19}\text{F}$  MRI exhibited not only high selectivity on cancer cells but also high sensitivity at a low nanoemulsion concentration of 26 pM.

Finally, a proof of concept in vivo study on the biocompatibility of NEs-RGD and its selective  $^{19}\text{F}$  MRI tumor detection was carried out. No acute toxicity was observed when NEs-RGD was intravenously injected to nude mice at a dose of 1780 mg/kg. Accumulation of NEs-RGD in liver was found through histopathological study. With  $^1\text{H}$  MRI as the background, intratumoral injection of NEs-RGD to an A549 xenograft nude mouse provided a hot spot  $^{19}\text{F}$  MRI image of the location and anatomy of tumor (Figure 5).

In summary, we have developed PFOB nanoemulsions with controllable particle sizes and multifunctionality for selective and sensitive detection of tumor cells with  $^{129}\text{Xe}$  hyper-CEST MRI,  $^{19}\text{F}$  MRI, and fluorescent imaging. The imaging system takes the advantage of high  $^{129}\text{Xe}$  solubility in PFOB and therefore generates  $^{129}\text{Xe}$  CEST signal. By integrating the highly sensitive  $^{129}\text{Xe}$  hyper-CEST MRI, highly selective  $^{19}\text{F}$  MRI, and convenient fluorescent imaging, the multimodal imaging system selectively and sensitively detects tumors cells in a versatile way on molecular, cellular, and animal levels. The

PFOB-based multimodal imaging system may provide a new strategy for accurate cancer diagnosis and therapy.

## ■ ASSOCIATED CONTENT

### 📄 Supporting Information

The Supporting Information is available free of charge on the ACS Publications website at DOI: 10.1021/acsabm.8b00635.

Detailed synthetic protocols of Cls-PEG-RGDyc and preparation and characterization of NEs and NEs-RGD, cellular uptake study and cytotoxicity assay, in vitro and in vivo <sup>19</sup>F-MRI, <sup>129</sup>Xe Hyper-CEST NMR and MRI, and H&E stains of NEs-RGD treated mice organs (PDF)

## ■ AUTHOR INFORMATION

### Corresponding Authors

\*E-mail: zxjiang@whu.edu.cn (Z.X.J.).

\*E-mail: xinzhou@wipm.ac.cn (X.Z.).

### ORCID

ZhongXing Jiang: 0000-0003-2601-4366

Xin Zhou: 0000-0002-5580-7907

### Author Contributions

†H.B.Z. and S.Z.C. contributed equally to this work.

### Notes

The authors declare no competing financial interest.

## ■ ACKNOWLEDGMENTS

This work was financially supported by the National Key R&D Program of China (2017YFA0505400, 2016YFC1304704), the National Natural Science Foundation of China (21402144, 21572168, and 81625011), the Key Research Program of Frontier Sciences, CAS (QYZDY-SSW-SLH018), and the Major Project of Technology Innovation Program of Hubei Province (2016ACA126).

## ■ REFERENCES

- Lee, H.; Lee, E.; Kim, D. K.; Jang, N. K.; Jeong, Y. Y.; Jon, S. Antibiofouling Polymer-Coated Superparamagnetic Iron Oxide Nanoparticles as Potential Magnetic Resonance Contrast Agents for In Vivo Cancer Imaging. *J. Am. Chem. Soc.* **2006**, *128*, 7383–7389.
- Gallagher, F. A.; Kettunen, M. I.; Day, S. E.; Hu, D.-E.; Ardenkjaer-Larsen, J. H.; in't Zandt, R.; Jensen, P. R.; Karlsson, M.; Golman, K.; Lerche, M. H.; Brindle, K. M. Magnetic Resonance Imaging of pH In Vivo Using Hyperpolarized (13)C-Labelled Bicarbonate. *Nature* **2008**, *453*, 940–943.
- Liang, X.; Li, Y.; Li, X.; Jing, L.; Deng, Z.; Yue, X.; Li, C.; Dai, Z. PEGylated Polypyrrole Nanoparticles Conjugating Gadolinium Chelates for Dual-Modal MRI/Photoacoustic Imaging Guided Photothermal Therapy of Cancer. *Adv. Funct. Mater.* **2015**, *25*, 1451–1462.
- Klippel, S.; Doepfert, J.; Jayapaul, J.; Kunth, M.; Rossella, F.; Schnurr, M.; Witte, C.; Freund, C.; Schroeder, L. Cell Tracking with Caged Xenon: Using Cryptophanes as MRI Reporters upon Cellular Internalization. *Angew. Chem., Int. Ed.* **2014**, *53*, 493–496.
- Riggle, B. A.; Wang, Y.; Dmochowski, I. J. A "Smart" Xe-129 NMR Biosensor for pH-Dependent Cell Labeling. *J. Am. Chem. Soc.* **2015**, *137*, 5542–5548.
- Walker, T. G.; Happer, W. Spin-Exchange Optical Pumping of Noble-Gas Nuclei. *Rev. Mod. Phys.* **1997**, *69*, 629–642.
- Zhou, X.; Sun, X. P.; Luo, J.; Zeng, X. Z.; Liu, M. L.; Zhan, M. S. Production of Hyperpolarized Xe-129 Gas Without Nitrogen by Optical Pumping at Cs-133 D-2 Line in Flow System. *Chin. Phys. Lett.* **2004**, *21*, 1501–1503.
- Zhou, X.; Graziani, D.; Pines, A. Hyperpolarized Xenon NMR and MRI Signal Amplification by Gas Extraction. *Proc. Natl. Acad. Sci. U. S. A.* **2009**, *106*, 16903–16906.
- Ward, K. M.; Aletras, A. H.; Balaban, R. S. A New Class of Contrast Agents for MRI Based on Proton Chemical Exchange Dependent Saturation Transfer (CEST). *J. Magn. Reson.* **2000**, *143*, 79–87.
- van Zijl, P. C. M.; Yadav, N. N. Chemical Exchange Saturation Transfer (CEST): What is in a Name and What Isn't? *Magn. Reson. Med.* **2011**, *65*, 927–948.
- Zeng, Q.; Guo, Q.; Yuan, Y.; Yang, Y.; Zhang, B.; Ren, L.; Zhang, X.; Luo, Q.; Liu, M.; Bouchard, L.-S.; Zhou, X. Mitochondria Targeted and Intracellular Biothiol Triggered Hyperpolarized Xe-129 Magnetofluorescent Biosensor. *Anal. Chem.* **2017**, *89*, 2288–2295.
- Jiang, Z.-X.; Liu, X.; Jeong, E.-K.; Yu, Y. B. Symmetry-Guided Design and Fluorous Synthesis of a Stable and Rapidly Excreted Imaging Tracer for (19)F MRI. *Angew. Chem., Int. Ed.* **2009**, *48*, 4755–4758.
- Yuan, Y.; Sun, H.; Ge, S.; Wang, M.; Zhao, H.; Wang, L.; An, L.; Zhang, J.; Zhang, H.; Hu, B.; Wang, J.; Liang, G. Controlled Intracellular Self-Assembly and Disassembly of F-19 Nanoparticles for MR Imaging of Caspase 3/7 in Zebrafish. *ACS Nano* **2015**, *9*, 761–768.
- Nakamura, T.; Sugihara, F.; Matsushita, H.; Yoshioka, Y.; Mizukami, S.; Kikuchi, K. Mesoporous Silica Nanoparticles for F-19 Magnetic Resonance Imaging, Fluorescence Imaging, and Drug Delivery. *Chem. Sci.* **2015**, *6*, 1986–1990.
- Lv, R.; Yang, P.; He, F.; Gai, S.; Li, C.; Dai, Y.; Yang, G.; Lin, J. A Yolk-like Multifunctional Platform for Multimodal Imaging and Synergistic Therapy Triggered by a Single Near-Infrared Light. *ACS Nano* **2015**, *9*, 1630–1647.
- Song, X.-R.; Wang, X.; Yu, S.-X.; Cao, J.; Li, S.-H.; Li, J.; Liu, G.; Yang, H.-H.; Chen, X. Co9Se8 Nanoplates as a New Theranostic Platform for Photoacoustic/Magnetic Resonance Dual-Modal-Imaging-Guided Chemo-Photothermal Combination Therapy. *Adv. Mater.* **2015**, *27*, 3285–3291.
- Bo, S.; Yuan, Y.; Chen, Y.; Yang, Z.; Chen, S.; Zhou, X.; Jiang, Z.-X. In Vivo Drug Tracking with F-19 MRI at Therapeutic Dose. *Chem. Commun.* **2018**, *54*, 3875–3878.
- Song, X.; Feng, L.; Liang, C.; Yang, K.; Liu, Z. Ultrasound Triggered Tumor Oxygenation with Oxygen-Shuttle Nanoperfluorocarbon to Overcome Hypoxia-Associated Resistance in Cancer Therapies. *Nano Lett.* **2016**, *16*, 6145–6153.
- Nishikami, Y.; Konishi, T.; Omoda, R.; Aihara, Y.; Oyaizu, K.; Nishide, H. Oxygen-Enriched Electrolytes Based on Perfluorochemicals for High-Capacity Lithium-Oxygen Batteries. *J. Mater. Chem. A* **2015**, *3*, 10845–10850.
- Song, G.; Liang, C.; Yi, X.; Zhao, Q.; Cheng, L.; Yang, K.; Liu, Z. Perfluorocarbon-Loaded Hollow Bi2Se3 Nanoparticles for Timely Supply of Oxygen under Near-Infrared Light to Enhance the Radiotherapy of Cancer. *Adv. Mater.* **2016**, *28*, 2716–2723.
- Klippel, S.; Freund, C.; Schroeder, L. Multichannel MRI Labeling of Mammalian Cells by Switchable Nanocarriers for Hyperpolarized Xenon. *Nano Lett.* **2014**, *14*, 5721–6.
- Stevens, T. K.; Ramirez, R. M.; Pines, A. Nanoemulsion Contrast Agents with Sub-picomolar Sensitivity for Xenon NMR. *J. Am. Chem. Soc.* **2013**, *135*, 9576–9579.
- Patrick, M. J.; Janjic, J. M.; Teng, H.; O'Hear, M. R.; Brown, C. W.; Stokum, J. A.; Schmidt, B. F.; Ahrens, E. T.; Waggoner, A. S. Intracellular pH Measurements Using Perfluorocarbon Nanoemulsions. *J. Am. Chem. Soc.* **2013**, *135*, 18445–18457.
- Temme, S.; Grapentin, C.; Quast, C.; Jacoby, C.; Grandoch, M.; Ding, Z.; Owenier, C.; Mayenfels, F.; Fischer, J. W.; Schubert, R.; Schrader, J.; Floegel, U. Noninvasive Imaging of Early Venous Thrombosis by F-19 Magnetic Resonance Imaging With Targeted Perfluorocarbon Nanoemulsions. *Circulation* **2015**, *131*, 1405–1414.
- Peng, Q.; Li, Y.; Bo, S.; Yuan, Y.; Yang, Z.; Chen, S.; Zhou, X.; Jiang, Z.-X. Paramagnetic Nanoemulsions with Unified Signals for

Sensitive <sup>19</sup>F MRI Cell Tracking. *Chem. Commun. (Cambridge, U. K.)* **2018**, *54*, 6000–6003.

(26) Rose, H. M.; Witte, C.; Rossella, F.; Klippel, S.; Freund, C.; Schroeder, L. Development of an Antibody-Based, Modular Biosensor for Xe-129 NMR Molecular Imaging of Cells at Nanomolar Concentrations. *Proc. Natl. Acad. Sci. U. S. A.* **2014**, *111*, 11697–11702.

(27) Shapiro, M. G.; Ramirez, R. M.; Sperling, L. J.; Sun, G.; Sun, J.; Pines, A.; Schaffer, D. V.; Bajaj, V. S. Genetically Encoded Reporters for Hyperpolarized Xenon Magnetic Resonance Imaging. *Nat. Chem.* **2014**, *6*, 629–634.

(28) Wang, Y.; Dmochowski, I. J. An Expanded Palette of Xenon-129 NMR Biosensors. *Acc. Chem. Res.* **2016**, *49*, 2179–2187.